Angle-Dependent Microresonator ESR Characterization of Locally Doped $Gd^{3+}:Al_2O_3$

I. S. Wisby,[1,2,*] S. E. de Graaf,[1] R. Gwilliam,[3] A. Adamyan,[4] S. E. Kubatkin,[4] P. J. Meeson,[2] A. Ya. Tzalenchuk,[1,2] and T. Lindström[1]

[1]*National Physical Laboratory, Hampton Road, Teddington TW11 0LW, United Kingdom*
[2]*Royal Holloway, University of London, Egham TW20 0EX, United Kingdom*
[3]*Advanced Technology Institute, Faculty of Electronics and Physical Sciences, University of Surrey, Guildford, Surrey GU2 7XH, United Kingdom*
[4]*Department of Microtechnology and Nanoscience, MC2, Chalmers University of Technology, SE-41296 Gothenburg, Sweden*

(Received 11 December 2015; revised manuscript received 14 July 2016; published 26 August 2016)

Interfacing rare-earth-doped crystals with superconducting circuit architectures provides an attractive platform for quantum memory and transducer devices. Here, we present the detailed characterization of such a hybrid system: a locally implanted rare-earth Gd^{3+} in Al_2O_3 spin system coupled to a superconducting microresonator. We investigate the properties of the implanted spin system through angular-dependent microresonator electron spin resonance (micro-ESR) spectroscopy. We find, despite the high-energy near-surface implantation, the resulting micro-ESR spectra to be in excellent agreement with the modeled Hamiltonian, supporting the integration of dopant ions into their relevant lattice sites while maintaining crystalline symmetries. Furthermore, we observe clear contributions from individual microwave field components of our microresonator, emphasizing the need for controllable local implantation.

DOI: 10.1103/PhysRevApplied.6.024021

I. INTRODUCTION

A reliable and scalable quantum-information architecture requires a quantum memory [1]. A promising route to realizing such a device lies in a hybrid approach, where the unique and desirable properties of a variety of independent physical systems are exploited in conjunction [2]. There has been particular interest in combining superconducting circuits with other two-level systems, including cold atoms and ions [3–5], two-level defects [6,7], molecules [8,9], and spin ensembles [10–13].

One system of particular interest for microwave quantum-memory applications is rare-earth (RE) ions doped into crystals [7,14–19]. These ion species are particularly promising, as their inner $4f$ optical electronic transitions have long coherence times [20]. Specific RE ions also have the potential for photon conversion between optical and microwave frequency bands for quantum-transducer applications [17,21].

For now, focus has turned to the requirement for a controllable and scalable infrastructure [1], leading to the development of local ion implantation [22,23] or specialist focused ion-beam [24] techniques for precision dopant control, which is not otherwise achievable from a growth process alone. With this in mind, we have previously demonstrated a local doping technique utilizing a hard nitride mask to create a locally defined RE spin system, whereby coupling to a superconducting microresonator was demonstrated on the order of 3 MHz [22]. While the potential of such a device was evident, it was ascertained from our work, along with that of others [25], that when employing such implantation techniques coupling strengths are limited by excessive linewidth broadening on the scale of ≈50–100 MHz.

In order to see such technology through to applications, it is imperative that we study these locally doped crystals and their structure in detail, on the scale at which coupling is mediated. This is, however, challenging due to the nature of local implantation, where the number of dopant ions is considerably lower (of the order of 10^{11}) than in grown, doped crystals. While techniques such as conventional electron spin resonance (ESR), photoluminescence, x-ray photoelectron spectroscopy, and secondary ion mass spectroscopy lack the sensitivity required to obtain measurements of such small spin ensembles, ultrasensitive microwave spectroscopy at millikelvin temperatures has shown more promise [18,22,26,27].

In this work, we explore the properties of an implanted gadolinium (Gd^{3+}) in Al_2O_3 spin system through angular-dependent microresonator ESR (micro-ESR) spectroscopy. We find the measured angular-dependent micro-ESR spectra to be in excellent agreement with the modeled Hamiltonian. This supports the conclusion that the dopant ions are well integrated into their relevant lattice sites and that crystalline symmetries are maintained. Furthermore, we observe clear contributions from individual microwave field components of our microresonator device, emphasizing the need for controllable

*ilana.wisby@npl.co.uk

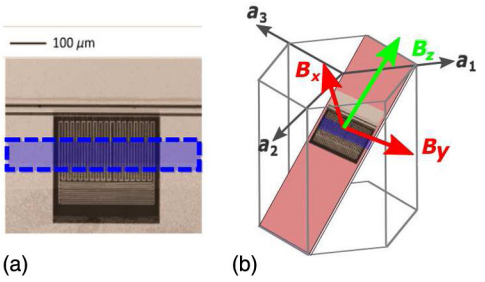

FIG. 1. (a) An optical image of the LE resonator used in this work. The device is inductively coupled to the transmission line and sits atop a region implanted with Gd^{3+} ions, which is highlighted for clarity with false coloring. (b) The sample is mounted and magnetic field aligned such that the R plane is parallel to the magnet B_z and B_y axes.

local implantation. By performing ultrasensitive, angle-resolved on-chip ESR we validate a complicated nano-engineered quantum system, thus paving the way for future applications.

The data shown in this work are obtained using a sample consisting of seven, frequency multiplexed, inductively coupled, NbN superconducting microresonators fabricated atop a systematically implanted Gd^{3+} rare-earth ion ensemble.

The focus of this work is on a lumped element (LE) resonator of center frequency $\omega_r/2\pi = 3.352$ GHz, which sits on an R-cut Al_2O_3 substrate with locally implanted Gd^{3+} in a 100×250-μm area [Fig. 1(a)]. The number of spins beneath the resonator is $N \approx 10^{11}$.

II. FABRICATION

The samples are fabricated utilizing a silicon-nitride mask technique which is detailed extensively in previous work [22] and briefly outlined as follows.

The local implantation process comprises initial deposition of alignment markers which are evaporated atop a commercial R-cut Al_2O_3 wafer. A SiN mask is next created to act as a stopping barrier for the incident ions during the ion implantation process, and is patterned such that only μm-size exposed windows are subject to implantation. The depth profile of the implanted ensemble can be altered by tuning the implantation energy and dose parameters. In our case, $^{160}Gd^{3+}$ is implanted at a dose of 1×10^{14} ions/cm^2 and an energy of 900 keV, giving a concentration profile with a peak implantation depth of 170 nm and full width at half maximum = 77 nm.

The contaminated SiN mask is removed and the implanted substrate annealed at 980 °C for 1 h to remove lattice defects and restore surface crystalline quality. A NbN thin film is then deposited and resonator devices are patterned with standard e-beam lithography techniques ensuring alignment to the implanted regions.

III. EXPERIMENT

The micro-ESR experiment is performed at mK temperatures in a dilution refrigerator fitted with a vector magnet. The system is equipped with heavily attenuated microwave lines and a low-noise cryogenic amplifier.

The magnetic-field axis is aligned such that the superconducting plane is parallel to the applied magnetic field B_z and B_y axes, as shown in Fig. 1(b). Initial characterization of the microresonator is performed using a vector network analyser (VNA) at $T \approx 10$ mK, with a power in the resonator of ≈3 pW. From S_{21} measurement we extract internal and coupled quality factors of $Q_i = 3.3 \times 10^5$ and $Q_c = 3.8 \times 10^4$, respectively—giving a zero field resonator dissipation rate of $\kappa/2\pi = 0.13$ MHz.

We next perform angular absorption spectroscopy at an enhanced $T = 250$ mK in order to observe higher-order transitions. An external static magnetic field (B_0) is applied in the R plane of the Al_2O_3 substrate and is rotated in this plane a full 360° in 4° intervals. We assume nominal 0° rotation where $B_0 = B_z$. For each B_0 rotation, we apply microwaves on resonance with our microresonator and step B_0 from 0–120 mT, tuning the spin-ensemble Zeeman transitions into resonance at spin-frequency degeneracies. At each B_0 step the local S_{21} minima are tracked and ${Q_m}^{-1} = {Q_i}^{-1} + {Q_c}^{-1}$ extracted from the S_{21} measurements.

The residual loss tangent due to the ions ($\tan\delta_{\text{ions}}$) is extracted from each absorption spectroscopy trace via numerical fitting of the total measured loss tangent: $\tan\delta_m = 1/Q_m = \tan\delta_c + \tan\delta_{\text{int}}$, where $\tan\delta_c$ is due to coupling to the transmission line. $\tan\delta_{\text{int}}$ are intrinsic losses attributable to a summation of the dielectric, magnetic field and losses due to the ions. From $\tan\delta_{\text{int}}$ we extract the field-dependent loss by subtracting the zero-field losses. The remaining $\tan\delta_B$ includes loss due to the ions, while other magnetic-field-induced losses are assumed to be negligible, such that $\tan\delta_B = \tan\delta_{\text{ions}}$.

An example of a single absorption spectroscopy trace for a B_0 rotation of 5° is shown in Fig. 2(a), where ESR's are observed as an additional absorption mechanism for the microwave photons. The measurement is done at power levels well below saturation to maximize sensitivity [28]. The total angular-dependent ESR spectra are shown in Fig. 2(b) as an intensity plot, where we have postprocessed the plot with an edge-detection filter to enhance the weaker transitions' locations for the reader's eye [29]—such that areas of high contrast correspond to ESR's.

For the results presented here, we couple to $N = 10^{11}$ spins, known from implantation, which provides a clear resonance signal. In the parallel field configuration we still see a clear signal despite coupling to 1/10th of those. It is interesting to compare this sensitivity to that of standard CW ESR techniques: Typically within CW ESR, an "ideal" $s = 1/2$ sample with a linewidth of 0.1 G yields a

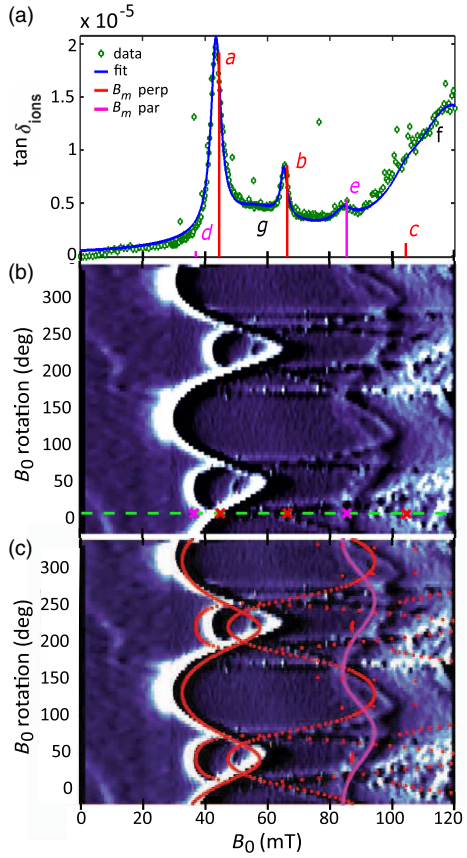

FIG. 2. (a) An individual absorption spectroscopy trace taken for B_0 rotated 5° [indicated by a green dashed line in (b)]. The $\tan\delta_{\text{ions}}$ data are shown (green). Numerical modeling of expected ESR degeneracy points in the perpendicular mode $B_{m,(a,b,c)} = 44$, 66, 104 mT (red) and the parallel mode $B_{m,(d,e)} = 37, 85$ mT (pink) are marked with relative amplitudes from modeling. Fitted overlay (blue)—summation of $Gd^{3+}:Al_2O_3$ transitions, impurities, and an additional unknown transition detailed in Table II. (b) Total angle-dependent ESR spectra intensity plot. The plot is postprocessed with the use of an edge-detection filter to highlight the transitions for the reader's eye. (c) As in Fig. 2(b), with additional marked expected peak positions calculated using numerical modeling: perpendicular mode (red) and parallel mode (pink).

sensitivity limit of 10^9, where the minimum number of spins detectable scales linearly with the linewidth. In our case the linewidth is 30 G (peak e), and as such is 300 times larger. Therefore, in the case of our spin system using our micro-ESR technique we are able detect less than 10^{10} spins, while a conventional ESR spectrometer would require at least 10^{12} spins. Or, in other words, here we detect 10^{10} spins, but using an ideal spin system we should be able to detect 10^7 spins.

IV. DISCUSSION

In order to understand our results, we examine the ESR spectra using the EasySpin [30] software package to model the angular dependence of the $Gd^{3+}:Al_2O_3$ system within our experimental parameters. We first consider the spin system and experimental parameters independently.

TABLE I. Ground-state crystal-field splitting parameters of $Gd^{3+}:Al_2O_3$ in MHz, used in modeling.

$b_2^0 = +3153$	$b_4^3 = 54.9$
$b_4^0 = 77.9$	$b_6^6 = 14.9$
$b_6^0 = 3.0$	$b_6^3 < 3.0$
$g = 1.9912$	

The spin system is described by the Hamiltonian

$$\mathcal{H} = g\mu_b BS + B_2^0 O_2^0 + B_4^0 O_4^0 + B_6^0 O_6^0 + B_4^3 O_4^3 + B_6^3 O_6^3 + B_6^6 O_6^6,$$

where O_k^q are Hermitian spin operators and B_k^q coefficients are real parameters. It is customary to redefine these B_k^q operators as

$$b_2^0 = 3B_2^0, \quad b_4^0 = 60B_4^0, \quad b_6^0 = 1260B_6^0,$$
$$b_4^3 = 3B_4^3, \quad b_6^3 = 36B_6^3, \quad b_6^6 = 1260B_6^6.$$

These coefficients have been previously determined experimentally through standard ESR measurements on grown $Gd^{3+}:Al_2O_3$ for comparable concentrations at 4.2 K [31,32]. These parameters are used in our Hamiltonian model (Table I), with minor (< 3%) adaptation of b_2^0 from +3123 to +3153 MHz for optimal fitting.

The Gd^{3+} substitutes into the two inequivalent Al sites of the Al_2O_3 of C_3 symmetry. Both sites share the same z axis, but are rotated about this axis by 60° with respect to each other. The spin system has a large zero-field splitting parameter $D = b_2^0$ attributable to the electric field produced by the O ions surrounding the Al sites.

The experimental conditions are governed by the geometry of the LE device, which results in a number of configurations between the static magnetic field (B_0) and oscillating microwave field component (B_{mw}). We begin by considering the case where B_0 is parallel to B_z, such that the current flowing within the microresonator inductor is either parallel or perpendicular to B_0 as depicted in Fig. 3(a). When the direction of current flow is parallel to B_0, B_{mw} is always perpendicular to B_0 [Fig. 3(a)(i)]. Where the direction of current flow is perpendicular to B_0, the B_{mw} components are either perpendicular or parallel to B_0 [Fig. 3(a)(ii)].

For modeling, we must transform the static crystal frame into the laboratory frame, accounting for the R-cut crystal. We therefore consider the relative translations of B_0 from the static crystal frame $[X_c Y_c Z_c]$ into the laboratory frame assuming a start position where $B_0 = Z_c$. In the case where current flow is parallel to B_0 [Fig. 3(a)(i)]: B_0 is brought

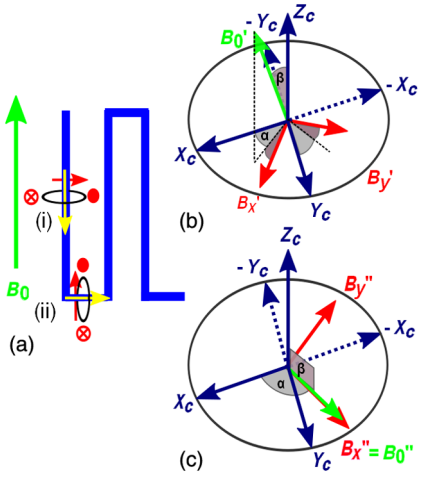

FIG. 3. (a) With B_0 (green) parallel to B_z, the current flowing in the microresonator inductor is either parallel (i) or perpendicular (ii) to B_0. We consider components of B_{mw} (red) for each case and relative orientation to B_0: (i) B_{mw} is perpendicular to B_0 in all components. (ii) B_{mw} is both perpendicular and parallel to B_0. (b) Vector diagram of transformation for case (i) of B_0 to B_0': $\alpha = 30$, $\beta = 33$, B_{mw} components are perpendicular. (c) Vector diagram of transformation for case (ii) of B_0 to B_0'': $\alpha = 120$, $\beta = 90$. B_{mw} is perpendicular to B_0 in B_y'' and parallel in B_x''.

into the laboratory frame by a transformation $[\alpha\,\beta\,\gamma] = [30\,33\,0]$ as shown in Fig. 3(b). The resulting B_0' is always perpendicular to the B_{mw} component in either B_x' or B_y'. In the case where current flows perpendicular to B_0 [Fig. 3(a)(ii)]: B_0 is brought into the laboratory frame by a transformation $[\alpha\,\beta\,\gamma] = [120\,90\,0]$ as shown in Fig. 3(c). The resulting B_0'' is both perpendicular and, importantly, parallel to B_{mw}'' components B_y'' and B_x'', respectively.

We numerically diagonalize our Hamiltonian for each of these operational modes for each B_0 rotation and find our model is in excellent agreement with the experimental data [Fig. 2(c)]. We find that the observed features of higher intensity within our experimental data correspond to operation where B_0 and B_{mw} components are perpendicular [red overlay in Fig. 2(c)]. The observed features of lower intensity within our experimental data correspond to a parallel B_0 and B_{mw} [pink overlay in Fig. 2(c)]. An example of this on a single trace is shown in Fig. 2(a), where modeled ESR transitions B_m are marked: $B_{m,(a,b,c)} = 44$, 66, 104 mT (red) and $B_{m,(d,e)} = 37$, 85 mT (pink), distinguished by perpendicular and parallel mode operation, respectively.

We can consider the relative areas within which the oscillating magnetic field is flowing both perpendicular and parallel to B_0 of $3400:832/2\ \mu\mathrm{m}^2 \approx 8.2:1$. We can compare this to the relative intensities of the ESR with the help of EasySpin. EasySpin returns intensities of each transition which are grouped according to parallel and perpendicular components. The parallel intensities are first fit to the measured spectra parallel component as nominal 1. The scaling factor for the perpendicular components required is next extracted and results in an intensity ratio of 8.75:1, which is accurate to within 10% of the value extracted from relative areas.

The resulting features of a single individual absorption trace can be fit with a convolution of functions where the spin ensemble and cavity are modeled as a single-mode harmonic oscillator [14]:

$$Q_m = \frac{\Delta^2 + \gamma^2}{2g_c^2\gamma + \kappa(\Delta^2 + \gamma^2)}\omega_r, \tag{1}$$

where Δ is the detuning from the fitted ESR transition B_f, κ is the cavity linewidth $= 0.13$ MHz, γ is the spin linewidth, and g_c is the collective coupling strength. An example of such a fit is overlaid atop an individual absorption spectroscopy trace in Fig. 2(a) (blue).

We fit the data using the numerically modeled ESR degeneracy center frequencies (B_m) as start points and constrain κ. We include two additional broad ESR features—the first potentially attributable to Fe^{3+} impurities in sapphire, which when modeled provides an ESR of $B_{m,f} = 119.9$ mT. The second is an unknown background feature previously observed in the literature at around 57 mT [22,26]. For the fit shown in Fig. 2(a) we extract the parameters detailed in Table II.

It is not surprising that we do not observe the $B_{m,d} = 37$ mT transition, since the expected relative intensity of this transition at $T = 250$ mK is very low. Neglecting $B_{m,d}$, we calculate the root-mean-square deviation between each B_m and B_f across the entire ESR spectra and find an average of 3% error. We believe this to be in excellent agreement, suggesting that the ions are successfully implanted and crystal structure retained.

Notably, our modeled system is obtained using parameters modified by $< 3\%$ from measurements obtained in grown Gd^{3+} in Al_2O_3 crystals [31]. This suggests good integration of the dopant ions into only the relevant lattice sites and that the expected system symmetries are maintained despite the high-energy, near-surface implantation.

In these and previous measurements of implanted rare-earth ion-superconductor systems, coupling strengths

TABLE II. Extracted parameters from fitting data with a convolution of Eq. (1). NA represents not applicable.

Peak	B_m (mT)	B_f (mT)	γ (MHz)	g_c (MHz)	System
a	44	43.4	53	4.5	$Gd^{3+}\perp$
b	66	65.4	34	1.8	$Gd^{3+}\perp$
c	104	104.3	150	2.1	$Gd^{3+}\perp$
d	47	37.1	NA	NA	$Gd^{3+}\parallel$
e	85	84.1	100	1.7	$Gd^{3+}\parallel$
f	119	120.0	450	3.0	Impurities: Fe^{3+}
g	NA	57.0	500	4.3	Unknown

have been limited by excessive linewidths [22,25]. It is interesting to note that we have not observed any dose dependence of these linewidths in complimentary measurements. The causes of such linewidth broadening can be manifold: indicative of inhomogeneous external fields, imperfections in the crystalline environment, i.e., poor site symmetry due to defects, or excessive spin-spin interactions [33].

As our experimental ESR's are in good agreement with our modeled system based on crystal-field parameters of grown Gd^{3+} in Al_2O_3 at similar concentrations [31], this suggests that dispersion arising from local defects in the crystalline environment may not be the primary cause of our excessive linewidth broadening. Notably, linewidth broadening is not observed within flip-chip devices coupled to superconducting microresonator devices where the relative distances between the two systems are large [34]. Neither is broadening prevalent when coupling to other types of cavities where superconducting structures are not present [35].

One possible explanation could be that local field distortions or crystal strain induced by the close proximity of the superconductor may be accountable for the linewidth broadening. It is interesting to note that we do not observe any angular dependence in the extracted linewidths and that the Gd^{3+} parallel contributions have larger linewidths, suggesting a greater relative inhomogeneity in the oscillating magnetic-field distribution due to the inductive meander turns.

It is also worth considering the impact of the resonator geometry on the resulting ESR spectra. We believe this further highlights the need for controllable local implantation techniques in order to create successful hybrid devices integrating spin ensembles and superconducting structures.

V. CONCLUSION

In conclusion, we demonstrate characterization of a locally implanted Gd^{3+} in the Al_2O_3 system utilizing angular-dependent microwave ESR spectroscopy at millikelvin temperatures. We find that, despite the high-energy and near-surface implantation, the resulting angular-ESR spectra are in excellent agreement with the modeled Hamiltonian parametrized by symmetries obtained from a grown Gd^{3+} in the Al_2O_3 system. These results support the successful integration of the dopant ions into their relevant lattice sites. We observe clear contributions from individual microwave field components of our microresonator, emphasizing the need for controllable local implantation when coupling spins to superconducting quantum architectures. We further demonstrate that angular-micro-ESR spectroscopy can provide an excellent means of studying even small numbers of spins, giving valuable feedback towards developing appropriate materials for future rare-earth-based quantum-information technologies.

ACKNOWLEDGMENTS

We thank J. Molloy, Y. Andreev, V. Atuchin, A. Zoladek-Lemanczyk, and D. Cox for fruitful discussions and support. This work was supported by the NMS, Swedish Research Council (VR) and Linneqs centre. Access to the IBC was supported by the EC program SPIRIT, Contract No. 227012.

[1] M. H. Devoret and R. J. Schoelkopf, Superconducting circuits for quantum information: An outlook, Science **339**, 1169 (2013).

[2] Ze-Liang Xiang, Sahel Ashhab, J. Q. You, and Franco Nori, Hybrid quantum circuits: Superconducting circuits interacting with other quantum systems, Rev. Mod. Phys. **85**, 623 (2013).

[3] B. B. Blinov, D. L. Moehring, L.-M. Duan, and Chris Monroe, Observation of entanglement between a single trapped atom and a single photon, Nature (London) **428**, 153 (2004).

[4] Wenjamin Rosenfeld, Stefan Berner, Jürgen Volz, Markus Weber, and Harald Weinfurter, Remote Preparation of an Atomic Quantum Memory, Phys. Rev. Lett. **98**, 050504 (2007).

[5] J. Verdú, H. Zoubi, Ch. Koller, J. Majer, H. Ritsch, and J. Schmiedmayer, Strong Magnetic Coupling of an Ultracold Gas to a Superconducting Waveguide Cavity, Phys. Rev. Lett. **103**, 043603 (2009).

[6] Matthew Neeley, M. Ansmann, Radoslaw C. Bialczak, M. Hofheinz, N. Katz, Erik Lucero, A. Oconnell, H. Wang, A. N. Cleland, and John M. Martinis, Process tomography of quantum memory in a Josephson-phase qubit coupled to a two-level state, Nat. Phys. **4**, 523 (2008).

[7] Abram L. Falk, Bob B. Buckley, Greg Calusine, William F. Koehl, Viatcheslav V. Dobrovitski, Alberto Politi, Christian A. Zorman, Philip X.-L. Feng, and David D. Awschalom, Polytype control of spin qubits in silicon carbide, Nat. Commun. **4**, 1819 (2013).

[8] Axel André, David DeMille, John M. Doyle, Mikhail D. Lukin, St. Ex Maxwell, Peter Rabl, Robert J. Schoelkopf, and Peter Zoller, A coherent all-electrical interface between polar molecules and mesoscopic superconducting resonators, Nat. Phys. **2**, 636 (2006).

[9] P. Rabl, D. DeMille, J. M. Doyle, M. D. Lukin, R. J. Schoelkopf, and P. Zoller, Hybrid Quantum Processors: Molecular Ensembles as Quantum Memory for Solid State Circuits, Phys. Rev. Lett. **97**, 033003 (2006).

[10] M. Steger, K. Saeedi, M. L. W. Thewalt, J. J. L. Morton, H. Riemann, N. V. Abrosimov, P. Becker, and H.-J. Pohl, Quantum information storage for over 180 s using donor spins in a ^{28}Si "Semiconductor vacuum", Science **336**, 1280 (2012).

[11] J. Twamley and S. D. Barrett, Superconducting cavity bus for single nitrogen-vacancy defect centers in diamond, Phys. Rev. B **81**, 241202 (2010).

[12] A. Imamoglu, Cavity QED Based on Collective Magnetic Dipole Coupling: Spin Ensembles as Hybrid Two-Level Systems, Phys. Rev. Lett. **102**, 083602 (2009).

[13] J. H. Wesenberg, A. Ardavan, G. A. D. Briggs, J. J.L Morton, R. J. Schoelkopf, D. I. Schuster, and K. Mølmer, Quantum Computing with an Electron Spin Ensemble, Phys. Rev. Lett. **103**, 070502 (2009).

[14] D. I. Schuster, A. P. Sears, E. Ginossar, L. DiCarlo, L. Frunzio, J. J. L. Morton, H. Wu, G. A. D. Briggs, B. B. Buckley, D. D. Awschalom, and R. J. Schoelkopf, High-Cooperativity Coupling of Electron-Spin Ensembles to Superconducting Cavities, Phys. Rev. Lett. **105**, 140501 (2010).

[15] C. Grezes, B. Julsgaard, Y. Kubo, M. Stern, T. Umeda, J. Isoya, H. Sumiya, H. Abe, S. Onoda, T. Ohshima, V. Jacques, J. Esteve, D. Vion, D. Esteve, K. Mølmer, and P. Bertet, Multimode Storage and Retrieval of Microwave Fields in a Spin Ensemble, Phys. Rev. X **4**, 021049 (2014).

[16] Y. Kubo, C. Grezes, A. Dewes, T. Umeda, J. Isoya, H. Sumiya, N. Morishita, H. Abe, S. Onoda, T. Ohshima, V. Jacques, A. Dreau, J. F. Roch, I. Diniz, A. Auffeves, D. Vion, D. Esteve, and P. Bertet, Hybrid Quantum Circuit with a Superconducting Qubit Coupled to a Spin Ensemble, Phys. Rev. Lett. **107**, 220501 (2011).

[17] S. Probst, H. Rotzinger, A. V. Ustinov, and P. A. Bushev, Microwave multimode memory with an erbium spin ensemble, Phys. Rev. B **92**, 014421 (2015).

[18] A. Bienfait, J. J. Pla, Y. Kubo, M. Stern, X. Zhou, C. C. Lo, C. D. Weis, T. Schenkel, M. L. W. Thewalt, D. Vion, D. Esteve, B. Julsgaard, K. Moelmer, J. J. L. Morton, and P. Bertet, Reaching the quantum limit of sensitivity in electron spin resonance, arXiv:1507.06831.

[19] S. Probst, H. Rotzinger, A. V. Ustinov, and P. A. Bushev, Microwave multimode memory with an erbium spin ensemble, Phys. Rev. B **92**, 014421 (2015).

[20] C. W. Thiela, T. Böttgerb, and R. L. Conea, Rare-earth-doped materials for applications in quantum information storage and signal processing, J. Lumin. **131**, 353 (2011).

[21] Christopher O'Brien, Nikolai Lauk, Susanne Blum, Giovanna Morigi, and Michael Fleischhauer, Interfacing Superconducting Qubits and Telecom Photons via a Rare-Earth-Doped Crystal, Phys. Rev. Lett. **113**, 063603 (2014).

[22] I. Wisby, S. E. de Graaf, R. Gwilliam, A. Adamyan, S. E. Kubatkin, P. J. Meeson, A. Ya. Tzalenchuk, and T. Lindström, Coupling of a locally implanted rare-earth ion ensemble to a superconducting micro-resonator, Appl. Phys. Lett. **105**, 102601 (2014).

[23] D. M. Toyli, C. D. Weis, G. D. Fuchs, T. Schenkel, and D. D. Awschalom, Chip-scale nanofabrication of single spins and spin arrays in diamond, Nano Lett., **10**, 3168 (2010).

[24] Nadezhda Kukharchyk, Shovon Pal, Jasper Rödiger, Arne Ludwig, Sebastian Probst, Alexey V. Ustinov, Pavel Bushev, and Andreas D. Wieck, Photoluminescence of focused ion beam implanted $Er^{3+}:Y_2SiO_5$ crystals, Phys. Status Solidi RRL **8**, 880 (2014).

[25] S. Probst, N. Kukharchyk, H. Rotzinger, A Tkalčec, A. D. Wieck, M. Siegel, A. V. Ustinov, P. A. Bushev, A. Tkalčec, and S. Wünsch, Hybrid quantum circuit with implanted erbium ions, Appl. Phys. Lett. **105**, 162404 (2014).

[26] Warrick G. Farr, Daniel L. Creedon, Maxim Goryachev, Karim Benmessai, and Michael E. Tobar, Ultrasensitive microwave spectroscopy of paramagnetic impurities in sapphire crystals at millikelvin temperatures, Phys. Rev. B **88**, 224426 (2013).

[27] H. Toida, Y. Matsuzaki, K. Kakuyanagi, X. Zhu, W. J. Munro, K. Nemoto, H. Yamaguchi, and S. Saito, Electron paramagnetic resonance spectroscopy using a direct current-SQUID magnetometer directly coupled to an electron spin ensemble, Appl. Phys. Lett. **108**, 052601 (2016).

[28] See Supplemental Material at http://link.aps.org/supplemental/10.1103/PhysRevApplied.6.024021 for an example of how the spectra changes with applied power.

[29] See Supplemental Material at http://link.aps.org/supplemental/10.1103/PhysRevApplied.6.024021 for a plot of the raw data.

[30] Stefan Stoll and Arthur Schweiger, EasySpin, a comprehensive software package for spectral simulation and analysis in EPR, J. Magn. Reson. **178**, 42 (2006).

[31] S. Geschwind and J. P. Remeika, Paramagnetic resonance of Gd^{3+} in Al_2O_3, Phys. Rev. **122**, 757 (1961).

[32] Paul H. E. Meijer and Jacques Lewiner, Energy levels, wave functions, dipole and quadrupole transitions of trivalent gadolinium ions in sapphire, J. Res. Natl. Bur. Stand. **75A**, 493 (1971).

[33] A. Abragam and B. Bleaney, *Electron Paramagnetic Resonance of Transition Ions* (Oxford University Press, Oxford, 1970).

[34] A. Tkalčec, S. Probst, D. Rieger, H. Rotzinger, S. Wünsch, N. Kukharchyk, A. D. Wieck, M. Siegel, A. V. Ustinov, and P. Bushev, Strong coupling of an Er^{3+}-doped $YAlO_3$ crystal to a superconducting resonator, Phys. Rev. B **90**, 075112 (2014).

[35] S. Probst, A. Tkalčec, H. Rotzinger, D. Rieger, J.-M. Le Floch, M. Goryachev, M. E. Tobar, A. V. Ustinov, and P. A. Bushev, Three-dimensional cavity quantum electrodynamics with a rare-earth spin ensemble, Phys. Rev. B **90**, 100404 (2014).